Computer simulation of RF liver ablation on an MRI scan data

N. Kosturski, S. Margenov, and Y. Vutov

Citation: AIP Conf. Proc. **1487**, 120 (2012); doi: 10.1063/1.4758949
View online: http://dx.doi.org/10.1063/1.4758949
View Table of Contents: http://proceedings.aip.org/dbt/dbt.jsp?KEY=APCPCS&Volume=1487&Issue=1
Published by the American Institute of Physics.

Computer Simulation of RF Liver Ablation on an MRI Scan Data

N. Kosturski, S. Margenov and Y. Vutov

Institute of Information and Communication Technologies – Bulgarian Academy of Sciences
25A Acad. G. Bonchev str., 1113 Sofia, Bulgaria

Abstract. Radio-frequency (RF) ablation is a low invasive technique for treatment of liver tumors. An RF-probe is inserted in the patient's liver and a ground pad is applied to the skin. Then the tumor is heated with RF current. The heat causes the destruction of tumor cells. We use the finite element method (FEM) to simulate and analyze various aspects of the procedure. A 3D image of the patient's liver is obtained from a magnetic resonance imaging (MRI) scan. Then, the geometry for the RF-probe and the ground pad is added. Our focus is on the influence of the position of the ground pads on the ablation process. Our simulation is based on an unstructured mesh. The size of the mesh is large due to the complexity of the domain. We discretize and solve the problem on a parallel computer using MPI for the parallelization. The presented numerical tests are performed on IBM Blue Gene/P machine at BGSC. The parallel efficiency of the incorporated BoomerAMG solver is demonstrated as well.

Keywords: RF ablation, numerical simulation, FEM, parallel algorithms
PACS: 02.60.Cb, 02.60.Dc, 02.60.Lj, 02.70.Dh, 87.50.st

INTRODUCTION

RF ablation is a well known technique for treatment of tumors, especially of metastatic ones in various organs. Tumor cells are destroyed through heating, caused by RF alternating current. An RF probe is placed percutaneously in the tumor and a ground pad is applied to the patient's skin. Despite the broad clinical experience in recent years, some aspects of the procedure are still under study. There is an ongoing research in design of the RF probes. Also, the right procedure parameters are vital for the successful outcome – killing all of the tumor cells, with minimal damage of the normal ones.

Computer simulation on geometry obtained from an MRI scan of the patient is performed. The influence of the position of the ground pads to the ablated volume is investigated. This in itself is interesting from the medical point of view. Moreover, in other computer simulations, *e.g.*, [1, 2, 3, 4], the position of the ground pad is neglected. Usually in those, the computational domain has a simple (cubic) shape. Assuming the pad is *far* from the probe, the zero potential condition is applied on the whole boundary of the domain. Our goal was to check the correctness of this kind of setup. We also compare the results of the ablation, in terms of ablated volumes, when ground pads are put in different positions.

The rest of the paper is organized as follows. In Section 2, the mathematical model of the bioheat equation is presented, along with its numerical treatment. In Section 3, we describe our computer simulation setup, and show the results. Finally, in section 4, we conclude with some concluding remarks.

THE MATHEMATICAL MODEL

Bioheat equation

The RF ablation procedure destroys the unwanted tissue by heating, arising when the energy dissipated by the electric current flowing through a conductor is converted to heat. The bio-heat time-dependent partial differential equation [2, 3]

$$\rho c \frac{\partial T}{\partial t} = \nabla \cdot k \nabla T + J \cdot E - \alpha h_{bl}(T - T_{bl}) \tag{1}$$

Application of Mathematics in Technical and Natural Sciences
AIP Conf. Proc. 1487, 120-126 (2012); doi: 10.1063/1.4758949

is used to model the heating process during the RF ablation. The term $J \cdot E$ in (1) represents the thermal energy arising from the current flow and the term $\alpha h_{bl}(T - T_{bl})$ accounts for the heat loss due to blood perfusion.

The following initial and boundary conditions are applied

$$\begin{array}{l} T = 310.15\,\mathrm{K}(37^{\circ}\mathrm{C}) \text{ when } t = 0 \text{ at } \Omega, \\ T = 310.15\,\mathrm{K}(37^{\circ}\mathrm{C}) \text{ when } t \geq 0 \text{ at } \partial\Omega. \end{array} \tag{2}$$

The following notations are used in (1) and (2):

- Ω – the entire domain of the model;
- $\partial\Omega$ – the boundary of the domain;
- ρ – density [kg/m^3];
- c – specific heat [J/kg K];
- k – thermal conductivity [W/m K];
- J – current density [A/m];
- E – electric field intensity [V/m];
- t – time [s];
- T – temperature [K];
- T_{bl} – blood temperature (310.15 K(37°C));
- w_{bl} – blood perfusion coefficient[s^{-1}];
- $h_{bl} = \rho_{bl} c_{bl} w_{bl}$ – convective heat transfer coefficient accounting for the blood perfusion in the model.
- α – tissue state coefficient

An important measure we use is the cumulative damage integral $\Psi(t)$, see [1]:

$$\Psi(t) = \ln\left(\frac{c(0)}{c(t)}\right) = A \int e^{-\frac{\Delta E}{RT(t)}}\, dt, \tag{3}$$

where $c(t)$ is the concentration of living cells, R is the universal gas constant, A is the "frequency" factor for the kinetic expression [s^{-1}], and ΔE is the activation energy for the irreversible damage reaction [J mol^{-1}]. The values used $A = 7.39 \times 10^{39}\mathrm{s}^{-1}$ and $\Delta E = 2.577 \times 10^5 \mathrm{J\ mol}^{-1}$ are taken from [1]. Tissue damage $\Psi(t) = 4.6$ corresponds to 99% probability of cell death. The value of $\Psi(t) = 1$, corresponding to 63% probability of cell death is significant, because at this point the tissue coagulation first occurs and blood perfusion stops. We account for the blood perfusion only in the liver by setting the tissue state coefficient α to zero in other tissues. In the liver α is set in accordance to the tissue damage at a point:

$$\begin{array}{lll} \alpha = e^{-\Psi(t)}, & when & \Psi(t) < 1 \\ \alpha = 0, & when & \Psi(t) \geq 1 \end{array} \tag{4}$$

The bio-heat problem is solved in two steps. The first step is to find the heat source $J \cdot E$. To do so, the distribution of the electric potential V is found by solving the Laplace equation:

$$\nabla \cdot \sigma \nabla V = 0, \tag{5}$$

with boundary conditions

$$\begin{array}{l} \nabla V = 0 \text{ at } \partial\Omega_f, \\ V = 0 \text{ at } \partial\Omega_{pad}, \\ V = V_0 \text{ at } \partial\Omega_{el}. \end{array}$$

The following notations are used in the above equations:

- V – Electric potential in Ω;
- σ – electric conductivity [S/m];
- V_0 – applied RF voltage;
- $\partial\Omega_{el}$ – surface of the conducting part of the RF probe.
- $\partial\Omega_{pad}$ – surface of the human body, where the ground pad is applied.
- $\partial\Omega_f = \partial\Omega \setminus \partial\Omega_{pad}$ – the rest of the body surface.

After determining the potential distribution, the electric field intensity and the current density can be computed from

$$E = -\nabla V, \qquad J = \sigma E.$$

To mimic the actual medical equipment, we need to determine the potential V_0 for the second boundary condition of (5) that will yield a given electrical output power P [W]. To do this, the Laplace equation is initially solved with an

arbitrary boundary condition $V = V_0^*$ at $\partial\Omega_{el}$. Then, E^* and J^* are obtained from the solution and the corresponding electrical power P^* can be computed as

$$P^* = \int_\Omega E^* \cdot J^* d\mathbf{x}.$$

Since the solution and all the components of E and J are proportional to the value of V_0 we can scale the obtained solution, instead of recomputing it, in the following way

$$V_0 = \lambda V_0^*, \quad E = \lambda E^*, \quad J = \lambda J^*, \quad \text{where} \quad \lambda = \sqrt{P/P^*}.$$

Let us note that this adjustment is performed only once in the beginning of the simulation. The obtained potential V_0 remains constant during the RF ablation procedure.

Numerical treatment

For the numerical solution of both of the above discussed steps of the simulation the finite element method in space is used ([5]). Linear conforming tetrahedral elements are used in this study, directly defined on the elements of the used unstructured mesh. This additionally provides for an optimal convergence rate and parallel scalability of the applied algebraic multigrid (AMG) preconditioner. To solve the bio-heat equation, after the space discretization, the time derivative is discretized via finite differences and the backward Euler scheme is used ([6]).

Let us denote with K^* the stiffness matrix coming from the FEM discretization of the Laplace equation (5). It can be written in the form

$$K^* = \left[\int_\Omega \sigma \nabla\Phi_i \cdot \nabla\Phi_j d\mathbf{x} \right]_{i,j=1}^N,$$

where $\{\Phi_i\}_{i=1}^N$ are the FEM basis functions.

The system of linear algebraic equations

$$K^* X = 0 \tag{6}$$

is to be solved to find the nodal values X of the potential distribution.

The electric field intensity and the current density are than expressed by the partial derivatives of the potential distribution in each finite element. This way, the nodal values F for the thermal energy $E \cdot J$ arising from the current flow are obtained.

Let us now turn our attention to the discrete formulation of the bio-heat equation. Let us denote with K and M the stiffness and mass matrices from the finite element discretization of (1). They can be written as

$$K = \left[\int_\Omega k \nabla\Phi_i \cdot \nabla\Phi_j d\mathbf{x} \right]_{i,j=1}^N,$$

$$M = \left[\int_\Omega \rho c \Phi_i \Phi_j d\mathbf{x} \right]_{i,j=1}^N.$$

Let us also denote with Ω_{bl} the subdomain of Ω where we account for the blood perfusion (the liver) and with M_{bl} the matrix

$$M_{bl} = \left[\int_\Omega \delta_{bl} h_{bl} \Phi_i \Phi_j d\mathbf{x} \right]_{i,j=1}^N,$$

where

$$\delta_{bl}(x) = \begin{cases} \alpha \text{ for } x \in \Omega_{bl}, \\ 0 \text{ for } x \in \Omega \setminus \Omega_{bl}. \end{cases}$$

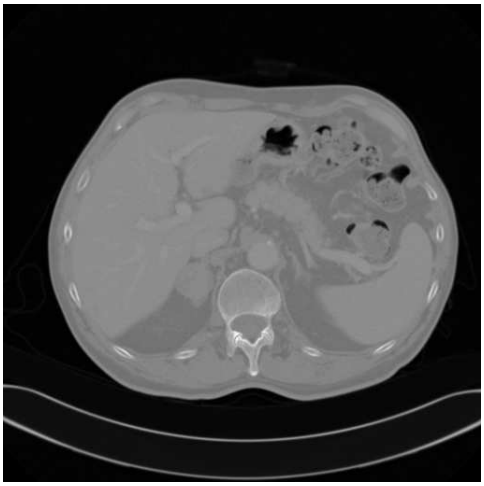

FIGURE 1. A slice from the MRI image

Than, the parabolic equation (1) can be written in matrix form as:

$$M\frac{\partial T}{\partial t}+(K+M_{bl})T=F+M_{bl}T_{bl}. \tag{7}$$

If we denote with τ the time-step, with T^{n+1} the solution at the current time level, and with T^n the solution at the previous time level and approximate the time derivative in (7) we obtain the following system of linear algebraic equations for the nodal values of T^{n+1}

$$AT^{n+1}=MT^n+\tau G, \tag{8}$$

where

$$A=M+\tau(K+M_{bl}) \quad \text{and} \quad G=F+M_{bl}T_{bl}.$$

The matrices K^* and A of the linear systems (6) and (8) are ill-conditioned and very large, having around 10^8 rows. Since they are symmetric and positive definite, we use the PCG [7] method, which is the most efficient solution method in this case. The stopping criterion used was

$$\frac{||R||_C}{||B||_C}<\varepsilon, \tag{9}$$

where ε is the given tolerance, R is the current residual, B is the right hand side of the linear system and $||X||_C \equiv (C^{-1}X,X)^{1/2}$, C is the preconditioner used. A parallel AMG implementation – BoomerAMG [8, 9] is used to precondition the linear systems. Since the matrix A does not vary much between time steps, we only construct the algebraic multigrid preconditioner once, before the first time-step. It can be readily used after that to precondition the linear systems for all subsequent time steps. We use the solution from the previous timestep as initial guess for the PCG method. This yields small number of iterations, when the solutions changes slowly with time.

COMPUTER SIMULATION

Experimental setup

Geometry data from a real patient was used for the computer simulation. The patient's 3D MRI image (see Figure 1) was taken from "3D Image Reconstruction for Comparison of Algorithm Database" (3D-IRCADb) [10]. The data set used was "3Dircadb1.4". It was already segmented by clinical experts, into different tissues. This very segmentation was used in our simulations. Some of the tissues, such as skin and bones, were combined, and not distinguished. The segmentation data was in the form of 3D image, where each voxel was given a number for a particular tissue.

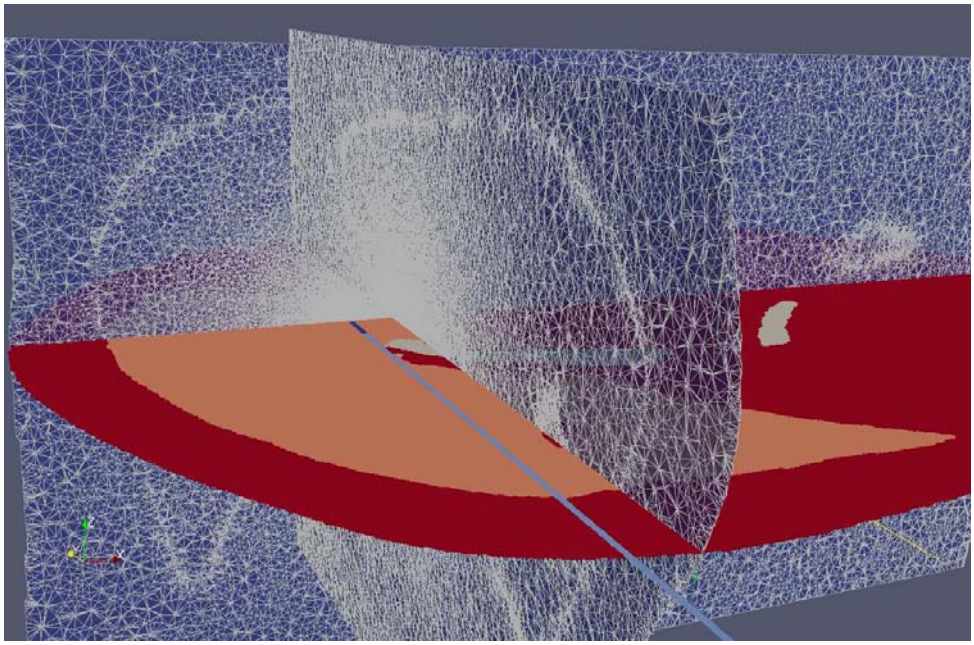

FIGURE 2. Inserted RF probe and finite element mesh

TABLE 1. Thermal and electrical properties of the materials

Material	ρ **[kg/m^3]**	c **[J/kg K]**	k **[W/m K]**	σ **[S/m]**
Stainless steel	7 013	405	71	4×10^8
Liver	1 060	3 600	0.512	0.333
Other tissues	1 060	3 600	0.512	0.333
Blood	1 000	4 180	0.543	0.667
Polyurethane	70	1 045	0.026	10^{-5}

The geometry for the RF probe was added directly into that image (see Figure 2). Then, the unstructured mesh was generated using the CGAL library [11]. The voxel image of the segmentation was directly fed into the library, and a tetrahedral mesh was produced. Local refinement was used near the electroconducting part of the RF probe, see Figure 1.

To simulate different ground pad positions, different boundary conditions (BCs) were applied. The corresponding BCs were incorporated in the mesh. This was performed by intersecting the body boundary with two spheres. The radiuses of the spheres and their position were chosen to produce intersections in different places, but with the same area. The area used was 12800 cm^2 – equal to the area of a real ground pad with sizes 160 cm $\times$ 80 cm. Figure 3 shows the considered positions of the ground pads. We also conducted a third simulation, where zero potential was applied to the entire boundary of the domain as usually done in existing studies. The three meshes differed only in the boundary conditions for the electrical part of the simulation.

We used IBM BlueGene/P Computer located in the Bulgarian Supercomputing Center. The parallelization approach is based on partitioning the meshes using ParMETIS [12, 13]. The partitioning is performed as a separate preprocessing step.

The conducting part of the RF probe is made from stainless steel, and the insulated one – from polyurethane. The physical properties of the materials used in our experiments are shown in Table 1. The value for blood perfusion coefficient $w_{bl} = 6.4^{-3}$ was taken from [1].

(a) (b)

FIGURE 3. (a) The ground pad in the front-left position and the RF probe; (b) The ground pad in the back position

TABLE 2. Ablated volumes

Applied power	5 W		7.5 W		10 W	
pad position	$V_1[cm^3]$	$V_{4.6}[cm^3]$	$V_1[cm^3]$	$V_{4.6}[cm^3]$	$V_1[cm^3]$	$V_{4.6}[cm^3]$
front	6.33	4.01	9.74	6.64	12.86	9.10
back	6.98	4.50	10.60	7.33	13.84	9.95
everywhere	7.87	5.18	11.79	8.28	15.25	11.14

Results

Three sets of experiments with varying electrical power applied were conducted. In all simulations the procedure was performed for 7 minutes. Table 2 shows the ablated volumes with different pad positions and different output power. With V_1 is denoted the volume, where $\Psi \geq 1$ and with $V_{4.6}$ — the volume with $\Psi \geq 4.6$ at the and of the procedure.

When we saw the non-trivial difference in the ablated volumes, the experiments were repeated with a higher PCG accuracy. The PCG accuracy ε was increased from 10^{-6} to 10^{-8}. This did not produce different results. In order to make sure that the difference was not caused by discretization errors, we performed additional tests with uniformly refined mesh and a smaller timestep. Each tetrahedron in the mesh was divided into 8 smaller ones. The timestep was decreased 4 times. The comparison is shown in Table 3 in the case of 10 W with and without refinement. With N is denoted the total number of unknowns, with P number of processors used for the solution, with N_{it} is denoted the total number of inner PCG iterations and finally the computing time in seconds is given. The number of the processors used was proportional to the number of the unknowns.

Second set of experiments show that the discretization error is insignificant. Using zero boundary conditions on the entire boundary produces 10% to 20% bigger ablated regions in all three cases. A 10% volume difference is observed between the front and back ground pad position cases, no matter the output power applied. This means, from the computation point of view, that the boundary conditions used have big influence on the results of the simulation. From the medical perspective, we see that the position of the ground pad is to be taken into account when, performing the procedure. For a particular effect one has to either move the ground pad, or adjust the ablation time and power.

Data for the execution time and number of processors used is also shown in Table 3. For our experiments, the number of the processors used were chosen to be proportional with the data size. Although the number of time steps is increased four times, the run time increase is less then four. The total number of inner PCG iterations is less than four times bigger for the lager problem. This is due to a smaller increase of the number inner PCG iterations. As the time step decreases the relative difference between the solutions in each time step gets smaller, and so are the inner PCG iterations. As a result we solve 32 times bigger problem on 8 times more CPUs for less then 4 times slower, which shows a good scalability of the method.

TABLE 3. Comparison with refined mesh, output power – 10W

pad position	N	P	timestep [s]	V_1	$V_{4.6}$	N_{it}	time [s]
front	2 183 424	128	5	12.857	9.102	642	1 723
front	17 467 392	1024	1.25	12.829	9.130	1 610	6 170
back	2 183 424	128	5	13.843	9.950	650	1 714
back	17 467 392	1024	1.25	13.864	9.978	1 635	6 179
everywhere	2 183 424	128	5	15.251	11.113	656	1 716
everywhere	17 467 392	1024	1.25	15.272	11.142	1 670	6 189

CONCLUDING REMARKS

We present a model of the RF ablation procedure along with a parallel implementation of the simulation. We use an unstructured mesh, based on the segmented MRI scan of a real liver.

We focused on the effect of the boundary conditions for the electrical part of the problem. The numerical results suggest that they strongly affect the outcome of the ablation procedure in terms of volume of malignant tissue destroyed. We further studied the numerical stability of our implementation to make sure that our results are valid.

The results suggest further exploration of the boundary condition is needed to better predict the RF ablation results. As the human body is very complex the exact electrical potential is hard to predict on the boundary of any considered subdomain. However, we question the assumption that applying zero potential to the whole boundary is realistic enough. Although the difference in the electrical field was small one in all experiments, significant differences in the result of the whole process are observed.

Some results showing the parallel efficiency of our implementation on the IBM Blue Gene/P machine are also presented.

ACKNOWLEDGMENTS

This work is partly supported by the Bulgarian NSF Grant DCVP 02/13. We would like to thank Professor Wolfgang Müller and Theodor Popov (AMET Ltd.) for their help, fruitful discussions and suggestions. We also kindly acknowledge the support of the Bulgarian Supercomputing Center for the access to the IBM Blue Gene/P supercomputer.

REFERENCES

1. Isaac A. Chang and Uyen D. Nguyen (2004) Thermal modeling of lesion growth with radiofrequency ablation devices, *BioMedical Engineering OnLine*, **3**, 27
2. S. Tungjitkusolmun, E.J. Woo, H. Cao, J.Z. Tsai, V.R. Vorperian, and J.G. Webster (2000) Medical and Biological Engineering and Computing **38**(5), 562–568.
3. S. Tungjitkusolmun, S.T. Staelin, D. Haemmerich, J.Z. Tsai, H. Cao, J.G. Webster, F.T. Lee, D.M. Mahvi, and V.R. Vorperian (2002) *IEEE transactions on biomedical engineering* **49**(1), 3–9.
4. N. Kosturski, S. Margenov, and Y. Vutov, "Comparison of Two Techniques for Radio-frequency Hepatic Tumor Ablation through Numerical Simulation," in *AIP CP* **1404**, Melville, NY, 2011, pp.431–437.
5. S. Brenner, and L. Scott, *The mathematical theory of finite element methods,* Texts in applied mathematics, **15**, Springer-Verlag, 1994.
6. E. Hairer, S.P. Norsett, and G. Wanner *Solving ordinary differential equations I, II*, Springer Series in Comp. Math., 2000, 2002
7. O. Axelsson, *Iterative Solution Methods*, Cambridge University Press, 1996.
8. V.E. Henson, and U.M. Yang, (2002) *Applied Numerical Mathematics* **41**(1), Elsevier, 155–177.
9. Lawrence Livermore National Laboratory, *Scalable Linear Solvers Project*, URL [2012] `http://www.llnl.gov/CASC/linear_solvers/`.
10. IRCAD, 3D Image Reconstruction for Comparison of Algorithm Database, URL [2012] `http://www.ircad.fr/softwares/3Dircadb/3Dircadb1/index.php?lng=en`
11. Computational Geometry Algorithms Library, URL [2012] `http://www.cgal.org/`
12. G. Karypis and V. Kumar, "A coarse-grain parallel multilevel k-way partitioning algorithm," in *Proceedings of the 8th SIAM conference on Parallel Processing for Scientific Computing,* 1997.
13. N. Kosturski, S. Margenov, and Y. Vutov, "Balancing the Communications and Computations in Parallel FEM Simulations on Unstructured Grids," in *9th international conference on Parallel Processing and Applied Mathematics,* PPAM 2011, Part II, (2012) *Lecture notes in computer science* **7204**, pp. 211–220, Springer.